

Amplifying the response of soft actuators by harnessing snap-through instabilities

Johannes T. B. Overvelde^a, Tamara Kloek^a, Jonas J. A. D'haen^a, and Katia Bertoldi^{a,b,1}

^aJohn A. Paulson School of Engineering and Applied Sciences, Harvard University, Cambridge, MA 02138; and ^bKavli Institute, Harvard University, Cambridge, MA 02138

Edited by John W. Hutchinson, Harvard University, Cambridge, MA, and approved July 21, 2015 (received for review March 11, 2015)

Soft, inflatable segments are the active elements responsible for the actuation of soft machines and robots. Although current designs of fluidic actuators achieve motion with large amplitudes, they require large amounts of supplied volume, limiting their speed and compactness. To circumvent these limitations, here we embrace instabilities and show that they can be exploited to amplify the response of the system. By combining experimental and numerical tools we design and construct fluidic actuators in which snap-through instabilities are harnessed to generate large motion, high forces, and fast actuation at constant volume. Our study opens avenues for the design of the next generation of soft actuators and robots in which small amounts of volume are sufficient to achieve significant ranges of motion.

soft actuator | snap-through instability | fluidic segment | amplification

The ability of elastomeric materials to undergo large deformation has recently enabled the design of actuators that are inexpensive, easy to fabricate, and only require a single source of pressure for their actuation, and still achieve complex motion (1–5). These unique characteristics have allowed for a variety of innovative applications in areas as diverse as medical devices (6, 7), search and rescue systems (8), and adaptive robots (9–11). However, existing fluidic soft actuators typically show a continuous, quasi-monotonic relation between input and output, so they rely on large amounts of fluid to generate large deformations or exert high forces.

By contrast, it is well known that a variety of elastic instabilities can be triggered in elastomeric films, resulting in sudden and significant geometric changes (12, 13). Such instabilities have traditionally been avoided as they often represent mechanical failure. However, a new trend is emerging in which instabilities are harnessed to enable new functionalities. For example, it has been reported that buckling can be instrumental in the design of stretchable soft electronics (14, 15), and tunable metamaterials (16–18). Moreover, snap-through transitions have been shown to result in instantaneous giant voltage-triggered deformation (19, 20).

Here, we introduce a class of soft actuators comprised of interconnected fluidic segments, and show that snap-through instabilities in these systems can be harnessed to instantaneously trigger large changes in internal pressure, extension, shape, and exerted force. By combining experiments and numerical tools, we developed an approach that enables the design of customizable fluidic actuators for which a small increment in supplied volume (input) is sufficient to trigger large deformations or high forces (output).

Our work is inspired by the well-known two-balloon experiment, in which two identical balloons, inflated to different diameters, are connected to freely exchange air. Instead of the balloons becoming equal in size, for most cases the smaller balloon becomes even smaller and the balloon with the larger diameter further increases in volume (Movie S1). This unexpected behavior originates from the balloons' nonlinear relation between pressure and volume, characterized by a pronounced pressure peak (21, 22). Interestingly, for certain combinations of interconnected balloons, such nonlinear response can result in snap-through instabilities at constant volume, which lead to significant and sudden changes of the membranes' diameters (Figs. S1 and S2). It is straightforward to show analytically that these instabilities can be triggered only if the pressure–volume relation of at least one of the membranes

is characterized by (i) a pronounced initial peak in pressure, (ii) subsequent softening, and (iii) a final steep increase in pressure (*Analytical Exploration: Response of Interconnected Spherical Membranes Upon Inflation*).

Highly Nonlinear Fluidic Segments

To experimentally realize inflatable segments characterized by such a nonlinear pressure–volume relation, we initially fabricated fluidic segments that consist of a soft latex tube of initial length L_{tube} , inner radius $R = 6.35$ mm, and thickness $H = 0.79$ mm. We measured the pressure–volume relation experimentally for three segments with $L_{tube} = 22 - 30$ mm, and found that their response is not affected by their length (Fig. S3). Moreover, the response does not show a final steep increase in pressure. This is because latex has an almost linear behavior, even at large strains.

Next, to construct fluidic segments with a final steep increase in pressure and a response that can be easily tuned and controlled, we enclosed the latex tube by longer and stiffer braids of length L_{braid} (Fig. 1A). It is important to note that the effect of the stiff braids is twofold. First, as $L_{braid} > L_{tube}$, the braids are in a buckled state when connected to the latex tube (Fig. 1B), and therefore apply an axial force, F , to the membrane. Second, at a certain point during inflation when the membrane and the braids come into contact, the overall response of the segments stiffens.

We derived a simple analytical model to predict the effect of L_{braid} and L_{tube} on the nonlinear response of these braided fluidic segments (*Simple Analytical Model to Predict the Response of the Fluidic Segments*). It is interesting to note that our analysis indicates that for a latex tube of given length, shorter braids lower the peak pressure due to larger axial forces (Fig. S4 C and E). Moreover, it also shows that L_{braid} strongly affects the volume at which stiffening occurs. In fact, the shorter the braids, the earlier contact between the braids and the membrane occurs, reducing the amount of supplied volume required to have a steep increase

Significance

Although instabilities have traditionally been avoided as they often represent mechanical failure, here we embrace them to amplify the response of fluidic soft actuators. Besides presenting a robust strategy to trigger snap-through instabilities at constant volume in soft fluidic actuators, we also show that the energy released at the onset of the instabilities can be harnessed to trigger instantaneous and significant changes in internal pressure, extension, shape, and exerted force. Therefore, in stark contrast to previously studied soft fluidic actuators, we demonstrate that by harnessing snap-through instabilities it is possible to design and construct systems with highly controllable nonlinear behavior, in which small amounts of fluid suffice to generate large outputs.

Author contributions: J.T.B.O. and K.B. designed research; J.T.B.O., T.K., and J.J.A.D. performed research; J.T.B.O., T.K., and K.B. analyzed data; and J.T.B.O. and K.B. wrote the paper.

The authors declare no conflict of interest.

This article is a PNAS Direct Submission.

¹To whom correspondence should be addressed. Email: bertoldi@seas.harvard.edu.

This article contains supporting information online at www.pnas.org/lookup/suppl/doi:10.1073/pnas.1504947112/-DCSupplemental.

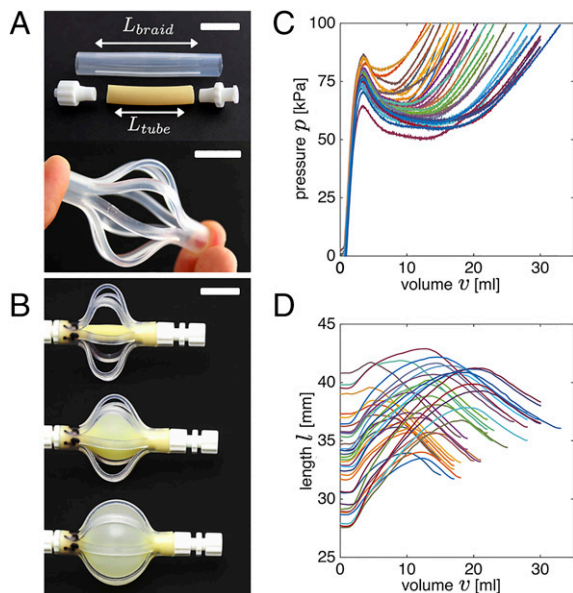


Fig. 1. (A) Outer and stiffer braids are added to the latex tube to create fluidic segments with highly nonlinear response. (B) Snapshots of a segment characterized by $(L_{braid}, L_{tube}) = (46, 20)$ during inflation at $v = 0, 10, 20$ mL. Evolution of (C) pressure (p) and (D) length (l) as a function of the supplied volume (v) for 36 fluidic segments characterized by $L_{braid} = 40 - 50$ mm and $L_{tube} = 20 - 30$ mm. (Scale bars: 10 mm.)

in pressure. Conversely, if L_{braid} is fixed, and the length of the membrane is varied, both the pressure peak and the volume at which stiffening occurs remain unaltered (Fig. S4F). However, in this case we find that shorter tubes lower the pressure of the softening region. Finally, the analytical model also indicates that the length of the fluidic segments, $l = \lambda_z L_{tube}$, initially increases upon inflation (Fig. S4E and F). However, when the tube and braids come into contact, further elongation is restrained by the braids and the segments shorten as a function of the supplied volume.

Having demonstrated analytically that fluidic segments with the desired nonlinear response can be constructed by enclosing a latex tube by longer and stiffer braids, and that their response can be controlled by changing L_{braid} and L_{tube} , we now proceed to fabricate such actuators. The stiffer braids are made from polyethylene-lined ethyl vinyl acetate tubing, with an inner radius of 7.94 mm and a thickness of 1.59 mm. Eight braids are formed by partly cutting this outer tube along its length guided by a 3D printed socket. Finally, Nylon Luer lock couplings (one socket and one plug) are glued to both ends of the fluidic segments to enable easy connection (Fig. 1A). We then measure their response experimentally by inflating them with water at a rate of 60 mL/min, ensuring quasi-static conditions (Fig. 1B and Movie S2).

We fabricated 36 segments with $L_{braid} = 40 - 50$ mm and $L_{tube} = 20 - 30$ mm. As shown in Fig. 1C, all fluidic segments are characterized by the desired nonlinear pressure—volume relation and follow the trends predicted by the analytical model (Fig. S4E and F). In particular, we find that for the 36 tested segments the initial peak in pressure ranges between 65 and 85 kPa (Fig. 1C). We also monitored the length of the segments during inflation (Fig. 1D). As predicted by the analytical model, we find that initially the segments elongate, but then shorten when the tube and braids come into contact. It is important to note that no instabilities are triggered upon inflation of the individual segments, because the supplied volume is controlled, not the pressure.

Combined Soft Actuator

Next, we created a new, combined soft actuator by interconnecting the two segments whose individual response is shown in Fig. 2A. Upon inflation of this combined actuator, very rich behavior

emerges (Fig. 2C and Movie S3). In fact, the pressure—volume response of the combined actuator is not only characterized by two peaks, but the second peak is also accompanied by a significant and instantaneous elongation. This suggests that an instability at constant volume has been triggered.

Numerical Algorithm. To better understand the behavior of such combined actuators, we developed a numerical algorithm that accurately predicts the response of systems containing n segments, based solely on the experimental pressure—volume curves of the individual segments. By using the 36 segments from experiments as building blocks, we can construct $36! / [(36 - n)n!]$ combined actuators comprising n segments (i.e., 630 different combined actuators for $n = 2$; 7,140 for $n = 3$; and 58,905 for $n = 4$), where we assume that the order in which we arrange the segments does not matter. It is therefore crucial to implement a robust algorithm to efficiently scan the range of responses that can be achieved.

We start by noting that, upon inflation, the state of the i th segment is defined by its pressure p_i and volume v_i , and its stored elastic energy can be calculated as

$$E_i(v_i) = \int_{V_i}^{v_i} p_i(\tilde{v}) d\tilde{v}, \quad [1]$$

in which we neglect dynamic effects. Moreover, V_i denotes the volume of the i th segment in the unpressurized state. When the

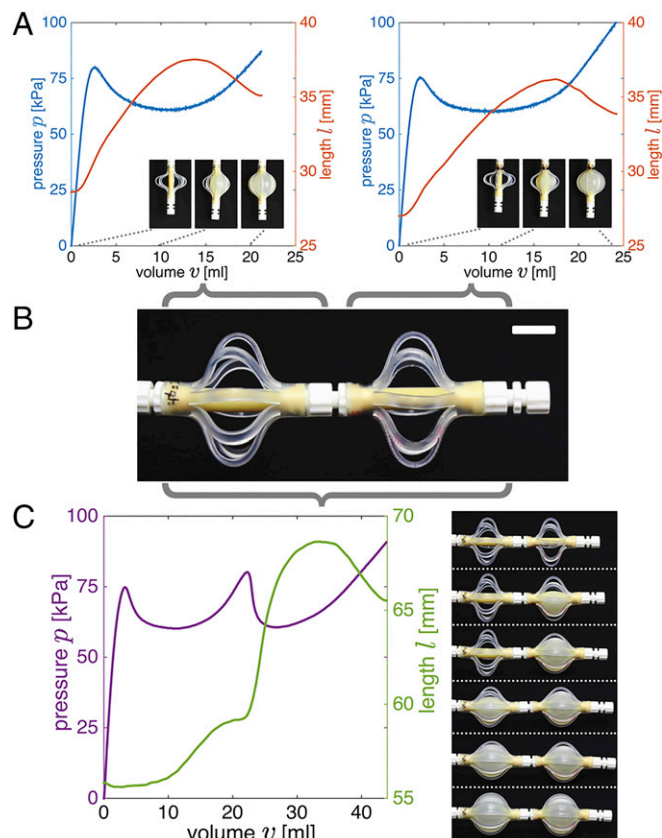


Fig. 2. (A) Evolution of pressure (p) and length (l) as a function of the supplied volume (v) for two fluidic segments characterized by $(L_{braid}, L_{tube}) = (46, 20)$ and $(46, 22)$ mm. Snapshots of the fluidic segments at $v = 0, 10, 20$ and $v = 0, 12, 24$ mL are shown as *Insets*, respectively. (B) The two fluidic segments are connected to form a new, combined soft actuator. (C) Evolution of pressure (p) and length (l) as a function of the supplied volume (v) for the combined actuator. Snapshots of the combined actuator at $v = 0, 9, 18, 27, 36, 45$ mL are shown as *Insets*.

total volume of the system, $v = \sum_{i=1}^n v_i$, is controlled (as in all our experiments), the response of the system is characterized by $n - 1$ variables v_1, \dots, v_{n-1} and the constraint

$$v_n = v - \sum_{i=1}^{n-1} v_i. \quad [2]$$

To determine the equilibrium configurations, we first define the elastic energy, E , stored in the system, which is given by the sum of the elastic energy of the individual segments

$$E(v_1, \dots, v_n) = \sum_{i=1}^n \int_{V_i} p_i(\tilde{v}) d\tilde{v}, \quad [3]$$

and use Eq. 2 to express the energy in terms of $n - 1$ variables

$$\tilde{E}(v_1, \dots, v_{n-1}) = \sum_{i=1}^{n-1} \int_{V_i} p_i(\tilde{v}) d\tilde{v} + \int_{V_n} p_n(\tilde{v}) d\tilde{v}. \quad [4]$$

Next, we implement a numerical algorithm that finds the equilibrium path followed by the actuator upon inflation (i.e., increasing v). Starting from the initial configuration (i.e., $v_i = V_i$), we incrementally increase the total volume of the system (v) and locally minimize the elastic energy (\tilde{E}). Because Eq. 4 already takes into account the volume constraint (Eq. 2), we use an unconstrained optimization algorithm such as the Nelder–Mead simplex algorithm implemented in Matlab (23). Note that this algorithm looks only locally for an energy minimum, similar to what happens in the experiments, and therefore it does not identify additional minima at the same volume that may appear during inflation.

Using the aforementioned algorithm, we find that for many actuators the energy can suddenly decrease upon inflation, indicating that a snap-through instability at constant volume has been triggered. To fully unravel the response of the actuators, we also detect all equilibrium configurations and evaluate their stability. The equilibrium states for the system can be found by imposing

$$\frac{\partial \tilde{E}}{\partial v_i} = 0, \quad \forall i \in \{1, \dots, n-1\}. \quad [5]$$

Substitution of Eq. 4 into Eq. 5, yields

$$\frac{\partial \tilde{E}}{\partial v_i} = p_i(v_i) - p_n \left(v - \sum_{j=1}^{n-1} v_j \right) = 0, \quad [6]$$

$$\forall i \in \{1, \dots, n-1\},$$

which, when substituting Eq. 2, can be rewritten as

$$p_1(v_1) = p_2(v_2) = \dots = p_n(v_n). \quad [7]$$

As expected, Eq. 7 ensures that the pressure is the same in all n segments connected in series.

Operationally, to determine all of the equilibrium configurations of a combined soft actuator comprising n fluidic segments, we first define 1,000 equispaced pressure points between 0 and 100 kPa. Then, for each of the n segments we find all volumes that result in those values of pressure (Fig. S5A). Finally, for each value of pressure, we determine the equilibrium states by making all possible combinations of those volumes (Fig. S5B). Note that by using Eq. 2 we can also determine the total volume in the system at each equilibrium state, and then plot the pressure–volume response for the combined actuator (Fig. S5C).

Finally, we check the stability of each equilibrium configuration. Because an equilibrium state is stable when it corresponds

to a minimum of the elastic energy \tilde{E} defined in Eq. 4, at any stable equilibrium solution the Hessian matrix

$$H(\tilde{E})(v_1, \dots, v_{n-1}) = \begin{bmatrix} \frac{\partial^2 \tilde{E}}{\partial v_1^2} & \dots & \frac{\partial^2 \tilde{E}}{\partial v_1 \partial v_{n-1}} \\ \vdots & \ddots & \vdots \\ \frac{\partial^2 \tilde{E}}{\partial v_{n-1} \partial v_1} & \dots & \frac{\partial^2 \tilde{E}}{\partial v_{n-1}^2} \end{bmatrix} \quad [8]$$

is positive definite. Note that the second-order partial derivatives in Eq. 8 can be evaluated as

$$\frac{\partial^2 \tilde{E}}{\partial v_i \partial v_j} = \begin{cases} p_i'(v_i) + p_n' \left(v - \sum_{k=1}^{n-1} v_k \right), & \text{if } i = j \\ p_n' \left(v - \sum_{k=1}^{n-1} v_k \right), & \text{if } i \neq j, \end{cases} \quad [9]$$

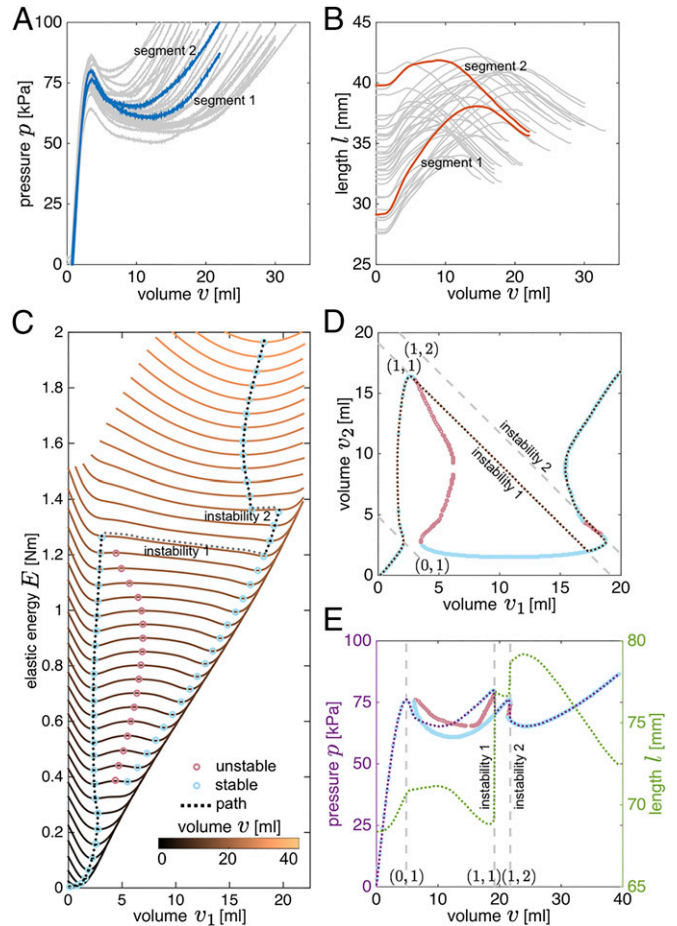


Fig. 3. (A) Experimentally measured pressure–volume relations for all 36 fabricated fluidic segments. (B) Experimentally measured length–volume relations for all 36 fabricated segments. (C) Numerically determined elastic energy, E , for a combined actuator comprising the two segments whose individual behavior is highlighted in A and B. The energy is shown for increasing values of the supplied volume, v . The stable and unstable equilibrium configurations are highlighted by blue and red circular markers, respectively. (D) Equilibrium configurations for the combined actuators. At $v = 19$ mL an unstable (1, 1) transition is found, resulting in a significant internal volume flow. A second instability of type (1, 2) is then triggered at $v = 22$ mL. (E) Numerically determined pressure–volume and length–volume relations for the combined soft actuator.

in which $p'_i(\bar{v}) = dp_i/d\bar{v}$. Taking advantage of the fact that all off-diagonal terms of the Hessian matrix are identical and using Sylvester's criterion (24), we find that an equilibrium state is stable if

$$\prod_{i=1}^k p'_i(v_i) + p'_n \left(v - \sum_{k=1}^{n-1} v_k \right) \sum_{i=1}^k \prod_{j=1, j \neq i}^k p'_j(v_j) > 0, \quad [10]$$

$$\forall k = 1, \dots, n-1.$$

Numerical Results. To demonstrate the numerical algorithm, we focus on two segments where the experimentally measured pressure–volume and length–volume responses are highlighted in Fig. 3A and B. In Fig. 3C we report the evolution of the total elastic energy of the system, E , as a function of the volume of the first segment, v_1 , for increasing values of the total supplied volume, v , and in Fig. 3D we show all equilibrium configurations in the v_1 – v_2 plane. We find that initially ($0 < v < 5$ mL) the volume of both segments increases gradually. However, for $5 < v < 19$ mL, v_1 remains almost constant and all additional volume that is added to the system flows into the second segment. Moreover, at $v = 6$ mL a second local minimum for E emerges, so that for $6 < v < 19$ mL the system is characterized by two stable equilibrium configurations. Although for $v > 13$ mL this second minimum has the lowest energy, the system remains in the original energy valley until $v = 19$ mL. At this point the local minimum of E in which the system is residing disappears, so that its equilibrium configuration becomes unstable, forcing the actuator to snap to the second equilibrium characterized by a lower value of E . Interestingly, this instability triggers a significant internal volume flow from the second to the first segment (Fig. 3D) and a sudden increase in length (Fig. 3E). Further inflating the system to $v = 22$ mL triggers a second instability, at which some volume suddenly flows back from the first to the second segment. After this second instability, increasing the system's volume further inflates both segments simultaneously.

All transitions that take place upon inflation (i.e., at $v = 5, 19$, and 22 mL) are highlighted by a peak in the pressure–volume curve (Fig. 3E), and correspond to instances at which one or more of the individual segments cross their own peak in pressure. These state transitions can either be stable or unstable (Fig. 3C–E). A stable transition always leads to an increase of the elastic energy stored in the system, and an instability results in a new equilibrium configuration with lower energy. Each state transition can therefore be characterized by the elastic energy release, which we define as a normalized scalar $\Delta \hat{E} = (E_{post} - E_{pre})/E_{pre}$. Here and in the following, the subscripts *pre* and *post* indicate the values of the quantity immediately before and after the state transition. Moreover, to better understand the effects of each transition on the system, we

define the associated normalized changes in internal volume distribution, length and pressure as $\Delta \hat{v} = \max(v_{i,post} - v_{i,pre})/V_{pre}$, $\Delta \hat{l} = (l_{post} - l_{pre})/l_{pre}$, and $\Delta \hat{p} = (p_{post} - p_{pre})/p_{pre}$.

In Fig. 4 we report $\Delta \hat{v}$, $\Delta \hat{l}$, and $\Delta \hat{p}$ versus the normalized change in energy, $\Delta \hat{E}$, for all transitions that occur in the 630 combined soft actuators comprising $n = 2$ segments. Note that there are more than 630 data points, because all actuators show two or more state transitions. We find that $-0.1 \leq \Delta \hat{E} \leq 4 \cdot 10^{-5}$, indicating that some of the transitions are stable (i.e., $\Delta \hat{E} > 0$), and others are unstable ($\Delta \hat{E} < 0$). We furthermore observe that the energy increase for stable transitions is very small, and is therefore sensitive to the increment size used in the numerical algorithm. By contrast, the elastic energy released during unstable transitions can be as high as 10% of the stored energy.

We also characterize each state transition according to the changes induced in the individual segments, and use (α, β) to identify the number of segments to the right of their pressure peak before (α) and after (β) the state transition. For combined soft actuators comprising $n = 2$ segments, the numerical results show three possible types of transitions: (0, 1), in which both segments are initially on the left of their peak in pressure and then one of them crosses its pressure peak during the state transition (blue markers in Fig. 4); (1, 2), in which the second segment also crosses its peak in pressure (green markers in Fig. 4); (1, 1), in which both segments cross their pressure peak, but one while inflating and the other while deflating (red markers in Fig. 4). We find that transitions of type (0, 1) occur in all combined actuators and are always stable. Therefore, the associated changes in elastic energy, length, pressure, and the internal volume distribution are approximately zero. By contrast, transitions of type (1, 1) are always unstable and result in both high elastic energy release (up to 10%) and high internal volume flow (up to 80%). Unlike (1, 1), transitions of type (1, 2) can be either stable or unstable. The unstable transitions result in moderate energy release (up to 2.5%), but can lead to significant and instantaneous changes in length (up to 14%). Therefore, our analysis clearly indicates not only that snap-through instabilities at constant volume can be triggered in soft fluidic actuators, but also that the associated released energy can be harnessed to trigger sudden changes in length, drops in pressure, and internal volume flows.

Experimental Results. To validate the numerical predictions, we measured experimentally the response of several combined actuators. In Fig. 5A we show the results for the system whose predicted transitions are indicated by the diamond gray markers in Fig. 4. We compare the numerically predicted and experimentally observed mechanical response, finding an excellent agreement. In particular, for this combined actuator we find that the pressure–volume curve is characterized by two peaks, indicating

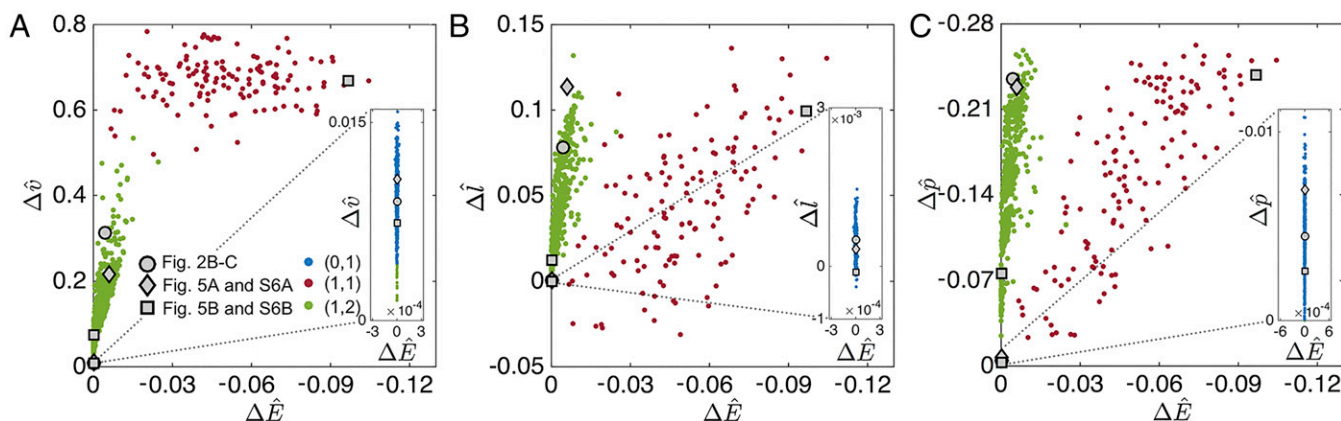


Fig. 4. A–C show $\Delta \hat{v}$, $\Delta \hat{l}$ and $\Delta \hat{p}$ versus the normalized change in energy $\Delta \hat{E}$ for all state transitions that occur in the 630 combined soft actuators comprising $n = 2$ fluidic segments. Blue, red, and green markers correspond to (0, 1), (1, 1), and (1, 2) transitions, respectively; (A) $\Delta \hat{v}$ versus $\Delta \hat{E}$; (B) $\Delta \hat{l}$ versus $\Delta \hat{E}$; and (C) $\Delta \hat{p}$ versus $\Delta \hat{E}$.

result, small compressors are sufficient to inflate these actuators, making them highly suitable for untethered applications.

Our results indicate that by combining fluidic segments with designed nonlinear responses and by embracing their nonlinearities, we can construct actuators capable of large motion, high forces, and fast actuation at constant volume. Although here we have focused specifically on controlling the nonlinear response of fluidic actuators, we believe that our analysis can also be used to enhance the response of other types of actuators (e.g., thermal, electrical and mechanical) by rationally introducing strong nonlinearities. Our approach therefore enables the design of a class of nonlinear systems that is waiting to be explored.

Materials and Methods

All individual soft fluidic segments and combined actuators investigated in this study are tested using a syringe pump (Standard Infuse/Withdraw PHD Ultra; Harvard Apparatus) equipped with two 50-mL syringes that have an accuracy of $\pm 0.1\%$ (1000 series, Hamilton Company). The segments and the combined actuators are inflated at a rate of 60 and 20 mL/min, respectively,

ensuring quasi-static conditions. Moreover, during inflation the pressure is measured using a silicon pressure sensor (MPX5100; Freescale Semiconductor) with a range of 0–100 kPa and an accuracy of $\pm 2.5\%$, which is connected to a data acquisition system (NI USB-6009, National Instruments). The elongation of the actuators is monitored by putting two markers on both ends of each actuator, and recording their position every two seconds with a high-resolution camera (D90 SLR, Nikon). The length of the actuator is then calculated from the pictures using a digital image processing code in Matlab. Each experiment is repeated 5 times, and the final response of the actuator as shown in the paper is determined by averaging the results of the last four tests. Finally, we measured the force exerted by the actuators during inflation when their elongation is completely constrained. In this case we use a uniaxial materials testing machine (model 5544A; Instron, Inc.) with a 100-N load cell to measure the reaction force during inflation.

ACKNOWLEDGMENTS. This work was supported by the Materials Research Science and Engineering Center under National Science Foundation Award DMR-1420570. K.B. also acknowledges support from the National Science Foundation (CMMI-1149456-CAREER) and the Wyss institute through the Seed Grant Program.

1. Laschi C, Mazzolai B, Mattoli V, Cianchetti M, Dario P (2009) Design of a biomimetic robotic octopus arm. *Bioinspir Biomim* 4(1):015006.
2. Ilievski F, Mazzeo AD, Shepherd RF, Chen X, Whitesides GM (2011) Soft robotics for chemists. *Angew Chem Int Ed Engl* 50(8):1890–1895.
3. Mosadegh B, et al. (2014) Pneumatic networks for soft robotics that actuate rapidly. *Adv Funct Mater* 24:2163–2170.
4. Martinez RV, et al. (2013) Robotic tentacles with three-dimensional mobility based on flexible elastomers. *Adv Mater* 25(2):205–212.
5. Martinez RV, Glavan AC, Keplinger C, Oyetibo AI, Whitesides GM (2014) Soft actuators and robots that are resistant to mechanical damage. *Adv Funct Mater* 24:3003–3010.
6. Roche ET, et al. (2014) A bioinspired soft actuated material. *Adv Mater* 26(8):1200–1206.
7. Majidi C (2013) Soft Robotics: A perspective—Current trends and prospects for the future. *Soft Robotics* 1:5–11.
8. Tolley MT, et al. (2014) A resilient, untethered soft robot. *Soft Robotics* 1:213–223.
9. Shepherd RF, et al. (2011) Multigait soft robot. *Proc Natl Acad Sci USA* 108(51):20400–20403.
10. Morin SA, et al. (2012) Camouflage and display for soft machines. *Science* 337(6096):828–832.
11. Kim S, Laschi C, Trimmer B (2013) Soft robotics: A bioinspired evolution in robotics. *Trends Biotechnol* 31(5):287–294.
12. Singamaneni S, Tsukruk V (2010) Buckling instabilities in periodic composite polymeric materials. *Soft Matter* 6:5681–5692.
13. Chen D, Yoon J, Chandra D, Crosby AJ, Hayward RC (2014) Stimuli-responsive buckling mechanics of polymer films. *J Polym Sci, B, Polym Phys* 52:1441–1461.
14. Rogers JA, Someya T, Huang Y (2010) Materials and mechanics for stretchable electronics. *Science* 327(5973):1603–1607.
15. Wang Y, et al. (2011) Super-elastic graphene ripples for flexible strain sensors. *ACS Nano* 5(5):3645–3650.
16. Shim J, Perdigo C, Chen ER, Bertoldi K, Reis PM (2012) Buckling-induced encapsulation of structured elastic shells under pressure. *Proc Natl Acad Sci USA* 109(16):5978–5983.
17. Florijn B, Coulais C, van Hecke M (2014) Programmable mechanical metamaterials. *Phys Rev Lett* 113(17):175503.
18. Wang P, Casadei F, Shan S, Weaver JC, Bertoldi K (2014) Harnessing buckling to design tunable locally resonant acoustic metamaterials. *Phys Rev Lett* 113(1):014301.
19. Keplinger C, Li T, Baumgartner R, Suo Z, Bauer S (2012) Harnessing snap-through instability in soft dielectrics to achieve giant voltage-triggered deformation. *Soft Matter* 8:285–288.
20. Li T, et al. (2013) Giant voltage-induced deformation in dielectric elastomers near the verge of snap-through instability. *J Mech Phys Solids* 61:611–628.
21. Miller JS (1952) Pressure within a bubble. *Am J Phys* 20:115.
22. Merritt DR, Weinhaus F (1978) The pressure curve for a rubber balloon. *Am J Phys* 46:976–977.
23. Lagarias JC, Reeds JA, Wright MH, Wright PE (1998) Convergence properties of the Nelder–Mead simplex method in low dimensions. *SIAM J Optim* 9:112–147.
24. Gilbert GT (1991) Positive definite matrices and Sylvester’s criterion. *Am Math Mon* 98:44–46.
25. Gent AN (1999) Elastic instabilities of inflated rubber shells. *Rubber Chem Technol* 72:263–268.
26. Kanner LM, Horgan CO (2007) Elastic instabilities for strain-stiffening rubber-like spherical and cylindrical thin shells under inflation. *Int J Non-Linear Mech* 42:204–215.
27. Weinhaus F, Barker W (1978) On the equilibrium states of interconnected bubbles or balloons. *Am J Phys* 46:978–982.
28. Dreyer W, Müller I, Strehlow P (1982) A study of equilibria of interconnected balloons. *Q J Mech Appl Math* 35:419–440.
29. Levin Y, da Silveira FL (2004) Two rubber balloons: Phase diagram of air transfer. *Phys Rev E Stat Nonlin Soft Matter Phys* 69(5 Pt 1):051108.
30. Müller I, Strehlow P (2004) *Rubber and Rubber Balloons: Paradigms of Thermodynamics*, Lecture Notes in Physics (Springer, New York).
31. Gent AN (1996) A new constitutive relation for rubber. *Rubber Chem Technol* 69:59–61.
32. Haughton D, Ogden R (1978) On the incremental equations in non-linear elasticity — ii. Bifurcation of pressurized spherical shells. *J Mech Phys Solids* 26:111–138.
33. Ertepinar A (1972) Theoretical and experimental studies on shells of arbitrary wall-thickness subjected to internal and external pressure. Ph.D. dissertation (Drexel University, Philadelphia).
34. Alexander H (1971) Tensile instability of initially spherical balloons. *Int J Eng Sci* 9:151–160.
35. Ogden R (1988) *Non-Linear Elastic Deformations* (Dover, New York).
36. Chater E, Hutchinson JW (1984) On the propagation of bulges and buckles. *J Appl Mech* 51:269–277.
37. Kyriakides S, Yu-Chung C (1990) On the inflation of a long elastic tube in the presence of axial load. *Int J Solids Struct* 26:975–991.
38. Kyriakides S, Yu-Chung C (1991) The initiation and propagation of a localized instability in an inflated elastic tube. *Int J Solids Struct* 27:1085–1111.

Supporting Information

Overvelde et al. 10.1073/pnas.1504947112

Analytical Exploration: Response of Interconnected Spherical Membranes Upon Inflation

To identify the key components in the design of an inflatable system that undergoes a snap-through instability upon inflation, we analytically explore the equilibrium states of two spherical membranes, connected in series. We start by describing the equations governing the response of a single hyperelastic spherical membrane upon inflation (25, 26), and then discuss the behavior of two interconnected spherical membranes (27–30).

Response of a Hyperelastic Spherical Membrane upon Inflation. We consider a spherical membrane with initial radius R , and initial thickness H , and assume that the membrane is thin (i.e., $H \ll R$), so that the contribution from bending and shear forces can be neglected. When the membrane is subjected to a uniform pressure p , a biaxial state of stress is achieved and the principal stretches are given by

$$\lambda_\theta = \lambda_\phi = \frac{r}{R}, \quad \lambda_r = \frac{h}{H}, \quad [\text{S1}]$$

r and h denoting respectively the radius and thickness of the membrane in the deformed configuration. Moreover, equilibrium requires

$$\sigma_\theta = \sigma_\phi = \frac{pr}{2h}, \quad [\text{S2}]$$

and the assumption of a plane stress condition yields

$$\sigma_r = 0, \quad [\text{S3}]$$

where σ_θ , σ_ϕ , and σ_r are the principal Cauchy stresses.

We consider the membrane to be made of a hyperelastic, incompressible material, the response of which is captured by the strain energy W . Because of incompressibility we have

$$\lambda_r = \frac{1}{\lambda_\theta \lambda_\phi}, \quad [\text{S4}]$$

and therefore the stress in the material is given by

$$\sigma_\theta = \sigma_\phi = \lambda_\theta \frac{\partial W(\lambda_\theta, \lambda_\phi)}{\partial \lambda_\theta}. \quad [\text{S5}]$$

Here, we model the material response using the incompressible Gent model (31), for which the strain energy is defined by

$$W(\lambda_\theta, \lambda_\phi) = -\frac{\mu J_m}{2} \log \left(1 - \frac{\lambda_\theta^2 + \lambda_\phi^2 + \lambda_\theta^{-2} \lambda_\phi^{-2} - 3}{J_m} \right), \quad [\text{S6}]$$

where μ is the initial shear modulus and J_m is a constant related to the strain saturation of the material (as the stresses become infinite when $J_m - \lambda_\theta^2 - \lambda_\phi^2 - \lambda_\theta^{-2} \lambda_\phi^{-2} + 3$ approaches zero). Note that the nonlinear pressure–volume response of an inflated spherical membrane depends greatly on the constitutive material model. Although in this study we have focused on a Gent model to achieve a final steep increase in pressure, when using a Varga, neo-Hookean, or three-term Ogden model no strain stiffening is observed upon inflation (32, 33). Although the

material parameters entering in the Ogden model can be tuned to account for strain stiffening or to even suppress the pressure peak encounter during inflation, here we preferred to use the Gent model because only μ and J_m need to be changed to control the nonlinear response (26).

Substitution of Eqs. S1, S2, and S6 into Eq. S5 yields

$$\sigma_\theta = \frac{pr}{2h} = \mu J_m \frac{\lambda_\theta^6 - 1}{-1 + \lambda_\theta^4(3 + J_m) - 2\lambda_\theta^6}, \quad [\text{S7}]$$

which can be rewritten as

$$\frac{pR}{\mu H} = \frac{2J_m}{\lambda^3} \frac{\lambda^6 - 1}{-1 + \lambda^4(3 + J_m) - 2\lambda^6}, \quad [\text{S8}]$$

where we use Eq. S4 to express h as a function of r (i.e., $h = HR^2/r^2$), and in which we set $\lambda = \lambda_\theta$ for convenience. Eq. S8 clearly shows that the initial radius R , initial thickness H , and shear modulus μ only scale the value of the pressure and that the only parameter that changes the shape of the $p - \lambda$ curve is the stretching limit J_m . Note that the volume inside the membrane can be easily determined as

$$v = \frac{4\pi}{3} (\lambda R)^3. \quad [\text{S9}]$$

As an example, in Fig. S1 we show the $p - v$ curves for three spherical membranes characterized by the same radius R and shear modulus μ and (a) H_a and $J_{m,a}$, (b) $H_b = 1.1H_a$ and $J_{m,b} = 0.9J_{m,a}$, and (c) $H_c = 1.05H_a$ and $J_{m,c} = 1.2J_{m,a}$.

It is important to note that in our analysis we assume that the deformation is homogeneous throughout the membrane, although it has been shown that this assumption can be violated by spherical membranes as they can exhibit asymmetric bifurcation modes (32, 34). However, these asymmetric modes do not affect the main features of the nonlinear pressure–volume relation typical for such membranes, and as such our analysis provides enough detail to qualitatively study the response of systems of interconnected membranes.

Response of Two Interconnected Spherical Membranes upon Inflation.

Having determined the pressure–volume curve for a single spherical membrane, we now determine the equilibrium states for a system of two interconnected membranes. For both membranes, we use the pressure–volume relation defined by Eqs. S8 and S9. Specialization of Eqs. 9 and 14 to a system comprising two spherical membranes, yields

$$v = v_1 + v_2, \quad [\text{S10}]$$

and

$$p = p_1 = p_2. \quad [\text{S11}]$$

Moreover, Eq. 17 reduces to

$$p_1'(v_1) + p_2'(v_2) > 0, \quad [\text{S12}]$$

so that an equilibrium configuration for a system comprising $n = 2$ spherical membranes is stable when

$$\sum_{i=1}^2 -\frac{2H_i\mu_i J_{m,i}}{R_i} \frac{3}{4\pi R_i} (\lambda_i R_i^3)^{-2/3} \times \frac{3 - 7(3 + J_{m,i})\lambda_i^4 + 21\lambda_i^6 + (3 + J_{m,i})\lambda_i^{10} - 6\lambda_i^{12}}{\lambda_i^4 (1 - (3 + J_{m,i})\lambda_i^4 + 2\lambda_i^6)^2} > 0, \quad [\text{S13}]$$

where λ_i indicates the stretch in the i th membrane. Moreover, H_i and R_i denote the initial thickness and radius of the i th membrane and μ_i and $J_{m,i}$ its shear modulus and strain saturation constant, respectively.

In Fig. S2 we show the response of the systems obtained by interconnecting membranes a and b (Fig. S2A), b and c (Fig. S2B), and a and c (Fig. S2C). Note that the pressure–volume curves for the individual segments are shown in Fig. S1. When connecting membranes a and b (Fig. S2A), upon inflation membrane a inflates first. Then, when this membrane starts to stiffen, membrane b also increases in volume. However, for this combined system all equilibrium points are stable. More interesting behavior is observed when combining membrane b and c (Fig. S2B). Initially, this system behaves similarly to the system shown in Fig. S2, with membrane c inflating first. However, at $v/V_a = 42$ a snap-through instability is triggered, resulting in a sudden decrease in pressure and increase in the diameter of membrane b . Therefore, at the instability a significant amount of volume flows from membrane c to membrane b . We also note that this system is characterized by equilibrium configurations that are disconnected from the main curve, so that they will never be reached upon inflation. Finally, even more complex behavior can be achieved by connecting membranes a and c (Fig. S2C). Here, a first instability causes all volume to flow from membrane a to membrane c , and a second instability forces some volume to flow back from membrane c to membrane a .

Simple Analytical Model to Predict the Response of the Fluidic Segments

The analytical predictions reported above reveal that snap-through instabilities at constant volume can be triggered in a system comprising interconnected spherical membranes only if the pressure–volume relation of at least one of the membranes is characterized by (i) a pronounced initial peak in pressure, (ii) subsequent softening, and (iii) a final steep increase in pressure. As for the case of the Gent model used in the previous analytical exploration, such response can be achieved by using membranes made of elastomeric materials that exhibit stiffening at large strains. However, it is important to note that commercially available latex tubes are characterized by an almost linear behavior, so that their response can be nicely captured using a neo-Hookean model (35), for which the strain energy is defined as

$$W(\lambda_1, \lambda_2, \lambda_3) = \frac{\mu}{2} (\lambda_1^2 + \lambda_2^2 + \lambda_3^2 - 3), \quad [\text{S14}]$$

where $\mu = 0.49$ MPa is the initial shear modulus of the latex material and λ_i are the principal stretches. Note that the neo-Hookean strain energy in Eq. S14 can be obtained from the Gent energy density in the limit as $J_m \rightarrow \infty$.

In the following, we first derive the pressure–volume relationship for a latex tube, and then we develop a simple analytical model to capture the response of the highly nonlinear braided fluidic segments used in this study.

Response of a Latex Tube Upon Inflation. We start by investigating analytically the response of a cylindrical latex membrane with initial radius R , initial length L_{tube} , and initial thickness H , and assume that the membrane is thin (i.e., $H \ll R$), so that the

contribution from bending and shear forces can be neglected. In particular, we determine the response when the membrane is inflated by an internal pressure p . For simplicity, we neglect end effects and local instabilities resulting from bulging (36–38), and assume that the cylindrical membrane deforms uniformly. The principal stretches are then given by

$$\lambda_\theta = \frac{r}{R}, \quad \lambda_z = \frac{l}{L_{tube}}, \quad \lambda_r = \frac{h}{H}, \quad [\text{S15}]$$

r , l , and h denoting the membrane's radius, length, and thickness in the deformed configuration, respectively. Moreover, as in experiments, we assume that the tube has closed ends, so that it is subjected to an axial force $p\pi r^2$. For such a membrane, equilibrium requires

$$\sigma_\theta = \frac{2prl}{2hl} = \frac{pr}{h}, \quad [\text{S16}]$$

$$\sigma_z = \frac{p\pi r^2}{2\pi rh} = \frac{pr}{2h}, \quad [\text{S17}]$$

and the assumption of plane stress conditions yields

$$\sigma_r = 0, \quad [\text{S18}]$$

where σ_i denote the principal Cauchy stresses.

We consider the membrane to be made of an incompressible neo-Hookean material (Eq. S14) and because of incompressibility we have

$$\lambda_r \lambda_\theta \lambda_z = 1. \quad [\text{S19}]$$

The stress in the material can then be expressed as

$$\sigma_r = \lambda_r \frac{\partial W}{\partial \lambda_r} - \tilde{p} = \mu \lambda_r^2 - \tilde{p} = 0 \quad \rightarrow \quad \tilde{p} = \mu \lambda_r^2, \quad [\text{S20}]$$

$$\sigma_\theta = \lambda_\theta \frac{\partial W}{\partial \lambda_\theta} - \tilde{p} = \mu (\lambda_\theta^2 - \lambda_r^2), \quad [\text{S21}]$$

$$\sigma_z = \lambda_z \frac{\partial W}{\partial \lambda_z} - \tilde{p} = \mu (\lambda_z^2 - \lambda_r^2), \quad [\text{S22}]$$

where \tilde{p} is a Lagrange multiplier. Substitution of Eqs. S15–S17 and S19 into Eqs. S21 and S22 yields

$$\frac{pR}{\mu H} = \lambda_z^{-1} - \lambda_r^4 \lambda_z, \quad [\text{S23}]$$

$$\frac{pR}{\mu H} = 2\lambda_r^2 \lambda_z (\lambda_z^2 - \lambda_r^2). \quad [\text{S24}]$$

Combining Eqs. S19, S23, and S24 results in

$$\lambda_r^{-2} \lambda_z^{-2} = 2\lambda_z^2 - \lambda_r^2, \quad [\text{S25}]$$

which can be solved to obtain

$$\lambda_r = \sqrt{\lambda_z^{-2} \sqrt{\lambda_z^8 - \lambda_z^2 + \lambda_z^2}}, \quad [\text{S26}]$$

where we used $\lambda_r \geq 1$ and $\lambda_z \geq 1$. Finally, substitution of Eq. S26 into Eq. S23 provides the evolution of the pressure as a function of the axial stretch λ_z

$$\frac{pR}{\mu H} = \lambda_z^{-1} - \left(\lambda_z^{-2} \sqrt{\lambda_z^8 - \lambda_z^2 + \lambda_z^2} \right)^2 \lambda_z. \quad [\text{S27}]$$

Note that the pressure–volume relationship for an inflated latex tube can be easily obtained from Eq. S27, because the volume enclosed by the membrane, v , is given by

$$v = l\pi r^2 = \pi \lambda_z L_{tube} \lambda_\theta^2 R^2 = \frac{\pi R^2 L_{tube}}{\lambda_z^3 + \sqrt{\lambda_z^6 - 1}}. \quad [\text{S28}]$$

In Fig. S3 we report the pressure–volume relation measured experimentally, and find excellent agreement with the analytical model (Eq. S27). Furthermore, we immediately see that no stiffening occurs, even for very high volumes. As a result, we do not expect to trigger any instability at constant volume in systems comprising interconnected latex tubes. Moreover, we also note that it is not possible to tune the pressure response of these inflatable tubes by changing their length, as the pressure does not depend on L_{tube} .

Response of a Braided Fluidic Segment. To construct fluidic segments with a final steep increase in pressure and whose response can be easily tuned and controlled, we enclosed the latex tube of initial length L_{tube} by longer and stiffer braids of initial length L_{braid} (Fig. 1A). The effect of the stiff braids is twofold: (i) as $L_{braid} > L_{tube}$, the braids have to be buckled first before attaching them to the latex tube, resulting in an axial force, F , applied to the membrane; (ii) at a critical point during inflation the braids come into contact with the latex tube, stiffening the response of the segment upon further inflation.

Effect of the axial force. To determine the effect of the braids on the initial response of the segments, we first estimate the axial force F introduced by n braids that enclose the latex tube. For the sake of simplicity, we model each individual braid as two rigid segments of length $L_{braid}/2$, connected by a torsional spring with stiffness K (Fig. S4A). As the braids are longer than the latex tube, before attaching them together, they are shortened by $u = L_{braid} - l = L_{braid} \sin \theta$ (Fig. S4B), causing them to buckle. Balance of the work done by the axial force F and the elastic energy requires

$$FL_{braid} \sin \theta = 2nK\theta, \quad [\text{S29}]$$

from which we obtain

$$F = \frac{2nK\theta}{L_{braid} \sin \theta}. \quad [\text{S30}]$$

For the fluidic segment considered in this study $\theta < 40^\circ$ we approximate $\sin \theta \approx \theta$, so that Eq. S30 reduces to

$$F \approx \frac{2nK}{L_{braid}}. \quad [\text{S31}]$$

Note that this approximation yields a constant axial force F , and introduces an error that is within 9%.

Finally, we experimentally estimate the torsional stiffness K by performing uniaxial compression tests on braids of different length and comparing the experimentally measured critical forces to Eq. S31. From the results reported in Fig. S4B we obtain that for the braids used in this study

$$K \approx L_{braid} \frac{-0.281L_{braid} + 20.4}{2n}. \quad [\text{S32}]$$

Next, we investigate the effect of the axial force F on the latex tube. To account for the axial force, Eq. S17 modifies as

$$\sigma_z = \frac{pr}{2h} + \frac{F}{2\pi rh}, \quad [\text{S33}]$$

so that Eq. S24 becomes

$$\frac{pR}{\mu H} = 2\lambda_r^2 \lambda_z (\lambda_z^2 - \lambda_r^2) - \frac{F\lambda_r^2 \lambda_z^2}{\pi \mu HR}, \quad [\text{S34}]$$

and Eqs. S16 and S23 remain unaltered. Note that Eq. S34 can also be used to estimate the axial stretch introduced into the tube by the braids in the unpressurized state (i.e., $p = 0$)

$$\lambda_{z,0} \geq \frac{1}{6} \left(c + \frac{\tilde{F}^2}{c} + \tilde{F} \right), \quad c = \sqrt[3]{\tilde{F}^3 + 6\sqrt{6}\sqrt{\tilde{F}^3 + 54} + 108}, \quad [\text{S35}]$$

in which $\tilde{F} = F/(\pi \mu HR)$.

By combining Eqs. S4, S23, and S34 we obtain

$$\lambda_r^{-2} \lambda_z^{-2} = 2\lambda_z^2 - \lambda_r^2 - \tilde{F} \lambda_z, \quad [\text{S36}]$$

from which the stretch in radial direction can be determined as

$$\lambda_r = \sqrt{\lambda_z^2 - \frac{\tilde{F}}{2} \lambda_z - \frac{\sqrt{(-2\lambda_z^4 + \tilde{F}\lambda_z^3)^2 - 4\lambda_z^2}}{2\lambda_z^2}}, \quad [\text{S37}]$$

where we assumed $\lambda_r \geq 0$ and $\lambda_z \geq \lambda_{z,0}$. By substituting Eq. S37 into Eq. S34 the pressure–axial stretch relationship is finally obtained as

$$\frac{pR}{\mu H} = \lambda_z^{-1} - \left(\lambda_z^2 - \frac{\tilde{F}}{2} \lambda_z - \frac{\sqrt{(-2\lambda_z^4 + \tilde{F}\lambda_z^3)^2 - 4\lambda_z^2}}{2\lambda_z^2} \right)^2 \lambda_z, \quad [\text{S38}]$$

and the relation between the volume and the axial stretch is given by

$$v = \frac{\pi L_{tube} R^2}{\lambda_z^3 - \frac{\tilde{F}}{2} \lambda_z^2 - \frac{1}{2} \sqrt{\lambda_z^4 (\tilde{F} - 2\lambda_z^2)^2 - 4}}, \quad [\text{S39}]$$

in which we assumed that $\lambda_z \geq 0$ and $\tilde{F} \geq 0$.

In Fig. S4C we show the analytically predicted pressure–volume curves for a latex tube of length $L_{tube} = 30$ mm subjected to an axial force $0 \leq F \leq g$ N (where $g = 9.81$ m s⁻¹ is the gravitational acceleration). As previously observed (37), the results show that an increase in the axial force applied to the membrane results in a lower peak pressure, indicating that the axial force resulting from the braids can be used to control the initial response of the fluidic segments. In Fig. S4C the analytical predictions (dashed lines) are also compared with experimental results (continuous lines) obtained inflating a latex tube of length $L_{tube} = 30$ mm with a weight attached to one of its ends. The good agreement between analytical and experimental results indicate that, despite the simplifications introduced in the derivation, our analysis captures all of the important features.

Effect of contact. At a critical point during inflation, the braids and the membrane come into contact, stiffening the overall response of the segments. Here, we assume that contact occurs when $v_{braid} = v$, where v_{braid} is the volume enclosed by the braids, which can be approximated as

$$v_{braid} = 2\pi \int_0^{1/2} (R + x \tan \theta)^2 dx \quad [\text{S40}]$$

$$= \frac{2\pi}{3 \tan \theta} \left(R + \frac{\lambda_z L_{tube} \tan \theta}{2} \right)^3 - \frac{2\pi R^3}{3 \tan \theta}$$

in which

$$\theta = \cos^{-1}(\lambda_z L_{tube} / L_{braid}). \quad [\text{S41}]$$

Because the pressure–volume relationship provided by Eqs. S38 and S39 is valid only for $v < v_{braid}$, we now proceed to determine how these modify after contact. We assume that the contact between the tube and the braids results in an uniform pressure, p_{braid} , applied to the braids (Fig. S4D). Because the beams are modeled as rigid, this pressure results in two effective forces with radial, F_r , and axial, F_a , components (Fig. S4D), given by

$$F_r = \frac{p_{braid} L_{braid}}{2} \cos \theta, \quad [\text{S42}]$$

and

$$F_a = \frac{p_{braid} L_{braid}}{4} \sin \theta. \quad [\text{S43}]$$

Balancing the external work and the elastic energy yields

$$\left(\frac{F_r}{2} + F - F_a \right) L_{braid} \sin \theta = 2nK\theta, \quad [\text{S44}]$$

where F is defined in Eq. S31. Furthermore, we assume that after contact the response is fully dominated by the braids so that

$$p = p_{braid} + \hat{p}, \quad [\text{S45}]$$

in which $\hat{p} = p(v_{braid} = v)$ can be calculated from Eqs. S38–S40. Finally, combining Eqs. S42–S45 we obtain

$$p = \frac{8nK\theta - 4FL_{braid} \sin \theta}{L_{braid}^2 (\cos \theta \sin \theta - \sin^2 \theta)} + \hat{p}. \quad [\text{S46}]$$

In Fig. S4E we show the predicted response for six segments characterized by $L_{tube} = 20$ mm and $L_{braid} = 40 - 50$ mm. The results indicate that for shorter braids, the peak in pressure is lower, demonstrating that the braids can be used to control the initial response of the fluidic segments. Moreover, the predicted response also clearly shows that L_{braid} strongly affects the volume at which stiffening occurs. In fact, the shorter the braids, the earlier contact between the braid and the membrane occurs, reducing the amount of volume that needs to be supplied to have a steep increase in pressure.

However, if the braid length is kept constant at $L_{braid} = 50$ mm and L_{tube} is varied ($L_{tube} = 20 - 30$ mm), both the pressure peak and the volume at which stiffening occurs remain unaltered (Fig. S4F). However, in this case we find that shorter tubes lower the pressure of the softening region. Finally, the analytical model also indicates that the length of the fluidic segments, $l = \lambda_z L_{tube}$, initially increases. However, when the tube and braids come into contact, further elongation is restrained by the braids and the segments shorten as a function of the supplied volume (Fig. S4E and F).

Therefore, this simple analytical model indicates that, by enclosing inflatable tubes with stiffer and longer braids, fluidic segments with the desired nonlinear response can be realized. Importantly, we have also found that by changing L_{braid} and L_{tube} their pressure–volume response (i.e., height of the initial pressure peak, softening response, and volume at which the final steep increase in pressure occurs) can be tuned and controlled. Therefore, we expect that by rationally interconnecting these braided fluidic segments, we can design systems in which snap-through instabilities at constant volume can be triggered.

Finally, it is important to note that we expect this model to predict only qualitatively and not quantitatively the response of the segments. This is mainly due to the effect of boundary conditions (i.e., the deformation is not uniform throughout the membrane) and inextensibility of the braids. Moreover, it has also been shown that local instabilities resulting in bulges (36–38) are triggered during the inflated of tubes. Although our model aims to provide design guidelines, accounting for all these effects would have lead to a significantly more complicated and less intuitive model, which falls outside the scope of this study.

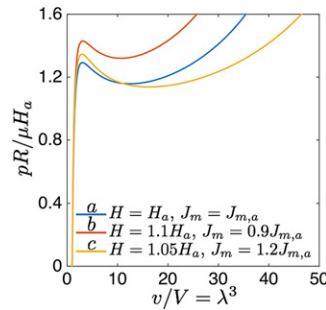
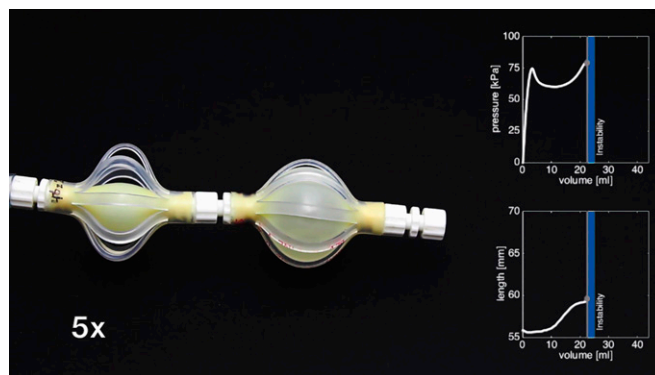


Fig. S1. Relation between the pressure and volume for three different hyperelastic spherical membranes upon inflation.



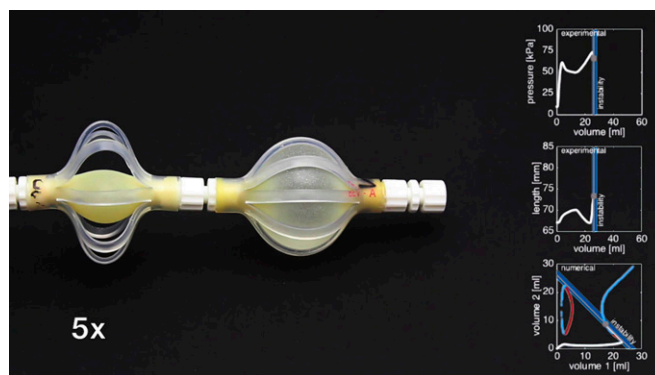
Movie S2. Inflation of a fluidic segment. Inflation of a single fluidic segment characterized by $L_{braid} = 46$ and $L_{tube} = 20$ mm. In the experiment, we inflated the segment with water at a rate of 60 mL/min.

[Movie S2](#)



Movie S3. Inflation of a combined soft actuator. Inflation of a combined soft actuator consisting of two interconnected fluidic segments, characterized by $(L_{braid}, L_{tube}) = (46, 20)$ and $(46, 22)$ mm. In the experiment, we inflated the segment with water at a rate of 20 mL/min. At $v = 23$ ml an instability at constant volume is triggered, causing a sudden increase in length, internal volume flow, and pressure drop.

[Movie S3](#)



Movie S4. Inflation of a combined soft actuator—sudden increase in length. Inflation of a combined soft actuator consisting of two interconnected fluidic segments, characterized by $(L_{braid}, L_{tube}) = (48, 30)$ and $(50, 20)$ mm. In the experiment, we inflated the segment with water at a rate of 20 mL/min. At $v = 26$ ml an instability at constant volume is triggered, causing a sudden increase in length of 10 mm, which corresponds to an increase of 11%.

[Movie S4](#)



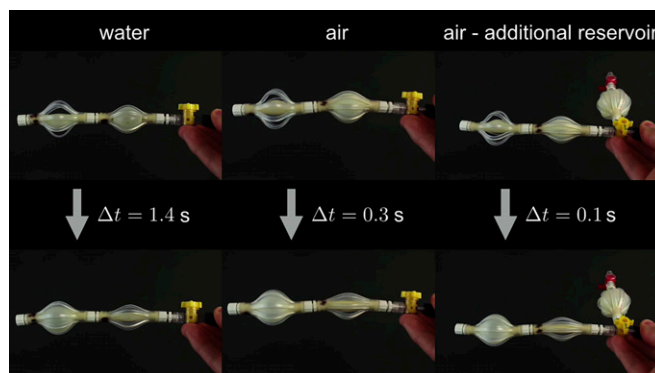
Movie S5. Inflation of a combined soft actuator—sudden internal volume flow. Inflation of a segment consisting of two interconnected fluidic segments, characterized by $(L_{braid}, L_{tube}) = (44, 30)$ and $(48, 26)$ mm. In the experiment, we inflated the segment with water at a rate of 20 mL/min. For this system two instabilities at constant volume are triggered. The first one occurs at $v = 16$ mL and results in the release of $\sim 10\%$ of the stored elastic energy and in a sudden internal volume flow. The second instability is triggered at $v = 24$ mL, causing some fluid to flow back.

[Movie S5](#)



Movie S6. Amplifying the response of a combined soft actuator comprising three fluidic segments. Amplification of the response of a combined soft actuator consisting of three interconnected fluidic segments, characterized by $(L_{braid}, L_{tube}) = (40, 28)$, $(44, 30)$, and $(50, 24)$ mm. We first inflate the actuator to $v = 28$ mL, and then decouple it from the syringe pump and connect it to a small reservoir containing only 1 mL of water. Remarkably, by adding only 1 mL of water to the system, we are able to trigger a significant internal volume flow of ~ 20 mL, that results in the deflation of two segments into one segment.

[Movie S6](#)



Movie S7. Actuation time. Actuation time for a soft actuator consisting of two interconnected fluidic segments, characterized by $(L_{braid}, L_{tube}) = (44, 30)$ and $(48, 26)$ mm. We first inflate the actuator to $v = 16$ mL, and then decouple it from the syringe pump and connect it to a small reservoir containing only 1 mL of water. When the system is inflated with water it takes more than 1 s for the changes in length, pressure, and internal volume induced by the instability to fully take place. By replacing water with air, the time is reduced from 1.4 s to 300 ms. Moreover, by adding an additional reservoir of air to increase the energy stored in the system, the actuation time can be further decreased to 100 ms.

[Movie S7](#)